

# Accurate Wavelength Tracking by Exciton Spin Mixing

Anton Kirch, Toni Bärschneider, Tim Achenbach, Felix Fries, Max Gmelch, Robert Werberger, Chris Guhrenz, Aušra Tomkevičienė, Johannes Benduhn, Alexander Eychmüller, Karl Leo, and Sebastian Reineke\*

Wavelength-discriminating systems typically consist of heavy benchtop-based instruments, comprising diffractive optics, moving parts, and adjacent detectors. For simple wavelength measurements, such as lab-on-chip light source calibration or laser wavelength tracking, which do not require polychromatic analysis and cannot handle bulky spectroscopy instruments, lightweight, easy-to-process, and flexible single-pixel devices are attracting increasing attention. Here, a device is proposed for monotonously transforming wavelength information into the time domain with room-temperature phosphorescence at the heart of its functionality, which demonstrates a resolution down to 1 nm and below. It is solution-processed from a single host–guest system comprising organic room-temperature phosphors and colloidal quantum dots. The share of excited triplet states within the photoluminescent layer is dependent on the excitation wavelength and determines the afterglow intensity of the film, which is tracked by a simple photodetector. Finally, an all-organic thin-film wavelength sensor and two applications are demonstrated where this novel measurement concept successfully replaces a full spectrometer.


## 1. Introduction

Wavelength-sensitive technologies are the basis for both monochromatic and polychromatic spectroscopy and are thus crucial

A. Kirch, T. Bärschneider, T. Achenbach, F. Fries, M. Gmelch, R. Werberger, A. Tomkevičienė, J. Benduhn, K. Leo, S. Reineke  
Dresden Integrated Center for Applied Physics and Photonic Materials (IAPP) and Institute for Applied Physics  
Technische Universität Dresden  
Nöthnitzer Straße 61, 01187 Dresden, Germany  
E-mail: sebastian.reineke@tu-dresden.de

C. Guhrenz, A. Eychmüller  
Physical Chemistry  
Technische Universität Dresden  
Zellescher Weg 19, 01069 Dresden, Germany

A. Tomkevičienė  
Department of Polymer Chemistry and Technology  
Kaunas University of Technology  
K. Barsausko g. 59, Kaunas 51423, Lithuania

 The ORCID identification number(s) for the author(s) of this article can be found under <https://doi.org/10.1002/adma.202205015>.

© 2022 The Authors. Advanced Materials published by Wiley-VCH GmbH. This is an open access article under the terms of the Creative Commons Attribution-NonCommercial License, which permits use, distribution and reproduction in any medium, provided the original work is properly cited and is not used for commercial purposes.

DOI: 10.1002/adma.202205015

for various fields of application, such as chemical material analysis, characterization of light sources, or calibration of monochromators and laser sources. Established techniques for realizing wavelength-selective light detection use one of two primary approaches: first, wavelength separation by an auxiliary structure,<sup>[1]</sup> i.e., a filter array or grating, where narrow light bands are directed onto individual pixels of a photodetector (PD) (array) with a broadband response; second, wavelength separation by the photoactive part itself, achieved by a multilayer arrangement of detectors, where every single detector is sensitive to a specific wavelength band.<sup>[2,3]</sup> Such spectroscopic devices commonly comprise solid hardware components that restrict them from versatile integration.

Recent developments, however, demonstrate both the huge drive and great potential in terms of easy-to-integrate,

low-cost, or lightweight applications,<sup>[4]</sup> e.g., narrowband photodiodes,<sup>[5–7]</sup> voltage-tunable Fabry–Pérot micro-interferometers,<sup>[8]</sup> or broadband sensors requiring wavelength multiplexing.<sup>[9]</sup> A smart approach to significantly reduce the device complexity was presented by Gautam et al.<sup>[10]</sup> A single-pixel and single-layer device was used to achieve a wavelength-sensitive photocurrent response that can discriminate red, green, and blue (RGB) values via the polarization of a polymer film in an aqueous surrounding. Only recently, a system was presented that consists of a multilayer single pixel of graded-bandgap perovskites evoking a wavelength-sensitive photocurrent response.<sup>[11]</sup>

Here, we present a single-chip wavelength sensor that exploits the dynamics of singlet and triplet states to discriminate a certain input signal. We employ a solution-processed host–guest system comprising organic room-temperature phosphors and fluorescent colloidal quantum dots (QDs), thereby introducing a new, promising application for organic room-temperature phosphorescence (RTP). The latter has been put to multifaceted use,<sup>[12]</sup> such as programmable luminescent tags,<sup>[13]</sup> oxygen sensing,<sup>[14]</sup> or moisture sensing.<sup>[15]</sup> Owing to their unique scalable optical properties, high quantum yield, and elevated photostability, colloidal quantum dots proved themselves valuable in a myriad of applications, like light-emitting diodes (LEDs),<sup>[16,17]</sup> solar cells,<sup>[18–20]</sup> or transistors.<sup>[21,22]</sup> Here, we present a single-layer approach that turns wavelength information into a distinct photocurrent response with a spectral resolution down to 1 nm and below while covering a wavelength range from 300 to 410 nm.

## 2. Results

### 2.1. Materials and Conception

Our material design intends to selectively mix excited singlet and triplet states in one active film. As introduced in previous studies from our lab, we use the very efficient organic phosphor 4,4'-dithianthrene-1-yl-benzophenone (BP-2TA) as an RTP emitter to generate triplet states.<sup>[23,24]</sup> The unmistakable fingerprint of triplet excited states is the long excited state lifetime (here about 30 ms) and afterglow transient, approximately seven orders of magnitude higher than in fluorescent emitters. Due to its tunable absorption edge, we decided to use CdSe/CdS core-shell QDs as a fluorescent emitter.<sup>[25]</sup> The reasoning is given in the subsequent sections. Employing a fluorescent, fast emitter with a lifetime on the nanosecond timescale does not contribute to an afterglow. Both the triplet- and singlet-emitting species are solved in anisole and toluene, respectively, and mixed with a poly(methyl methacrylate) (PMMA) host matrix solution to suppress nonradiative exciton quenching of the triplet states.<sup>[26]</sup> The photoactive layer is drop-cast onto a quartz glass substrate from solution (Figure 1a) in order to achieve a high film thickness while the other photo-physical properties remain stable.<sup>[27]</sup> The film thickness ranges around 25 μm (see the Supporting Information for details). The recipe was adopted after screening a range of emitters and concentrations yielding high phosphorescent photoluminescence (PL) intensity, as presented in refs. [24,28].

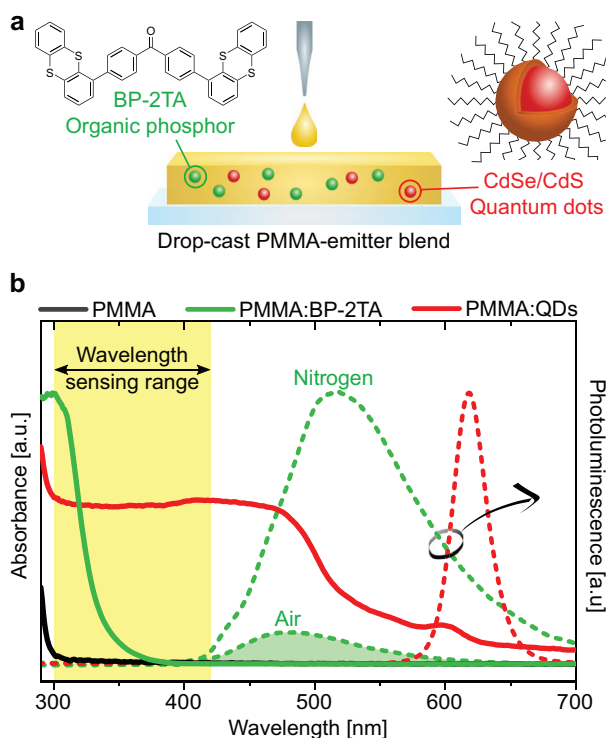


**Figure 1.** Materials and their optical characteristics. a) Materials used in the wavelength-sensing layer. b) Their respective absorbance (solid lines) and CW photoluminescence emission (dashed lines) profiles. The weak singlet emission of BP-2TA in air (shaded with green) is also shown. Within the indicated range (shaded with yellow), the share of RTP emission under illumination can be tuned by excitation wavelength.

Figure 1b shows the absorbance (solid lines) and PL emission profiles (dashed lines) under continuous-wave (CW) excitation at 365 nm of both light-emitting species in PMMA. The host PMMA is not photoactive in the region of interest, as indicated by its flat black absorbance line. The absorbance characteristics of the red-emitting QDs are about constant between 300 and 450 nm. Their sharp emission feature just above 600 nm originates from bright excited states that can be understood as being of singlet-like nature, as they show prompt fluorescence<sup>[25,29]</sup> (cf., Section S1, Supporting Information). Despite spin being no appropriate quantum number to describe excited states in semiconductor QDs,<sup>[30]</sup> we herein call the origin of the QD emission singlet-like excitons for the sake of discriminating them from the long-living triplet excited states of the green-emitting organic phosphor. The absorbance of the latter peaks at 300 nm and tails off toward 400 nm. Its emission predominantly originates from excited triplet excitons, and only a minor contribution can be attributed to its singlet states, as can be seen from its CW PL emission in air (shaded in green) and nitrogen atmosphere in Figure 1b. According to previous results published from our lab, the fluorescence PL quantum yield (PLQY) at 365 nm excitation ranges around 1% while its phosphorescence PLQY reaches 20%, which renders the molecule an efficient organic phosphor.<sup>[28]</sup>

Absorption of excitation light by BP-2TA produces a few singlet ( $S_{RTP}$ ) but mostly triplet excited states ( $T_{RTP}$ ) by efficient intersystem crossing in the steady state. The absorption of excitation light by the quantum dots produces singlet-like excited states ( $S_{QD}$ ). Within the indicated range of wavelength sensing, cf., the yellow shaded area in Figure 1b, the ratio of quantum dot-to-phosphor absorbance is gradually increasing with excitation wavelength. Assuming moderate excitation densities, where nonlinear effects like annihilation processes do not dominate the exciton dynamics, the relative share of the organic triplet exciton density ( $T_{RTP}$ ) to the sum of all luminescent excited state densities ( $T_{RTP} + S_{RTP} + S_{QD}$ ) within the photoactive film, henceforth called the “spin mixing ratio (SMR),” becomes thus a function of excitation wavelength

$$SMR = SMR(\lambda_{ex}) = \frac{T_{RTP}}{T_{RTP} + S_{RTP} + S_{QD}} \quad (1)$$

This reasoning elucidates our motivation to choose QDs as fluorescent materials in the first place. Unlike many organic fluorescent emitters, QDs have very steady absorption characteristics above their absorption edge, which can be easily tuned by dot size. Together with the slope of the RTP emitter, the system is bound to enable a monotonous function  $SMR(\lambda_{ex})$  within the shaded area in Figure 1b.

### 2.2. Setup and Results

As shown in Figure 2b, the film is excited with a white xenon lamp that is connected to a monochromator, which is set to integer wavelength values. An optical beam shutter cuts off the excitation light to record the off-cycle response of the film. All measurements are conducted at room temperature and under nitrogen atmosphere to prevent triplet quenching by oxygen. The PL intensity of the film is recorded using an amplified

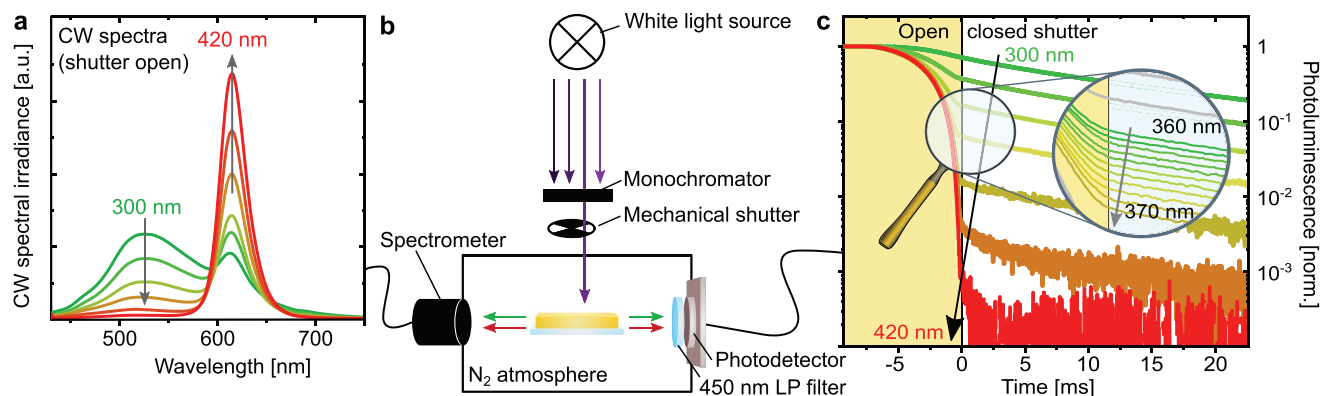


**Figure 2.** Experimental setup for single-film wavelength sensing. a) PL spectrum of the film depending on the excitation wavelength, trend indicated by arrows. b) Sketch of the experimental setup. c) Specific excitation wavelengths create distinct off-cycle transients. Inset: Even excitation wavelength steps of 1 nm can be discriminated. To keep the figures clear, not all measured transients and spectra are displayed. The transients are averaged ten times ( $n = 10$ ).

silicon PD. To exclude any influence of residual UV excitation light, the detector is covered with a 450 nm longpass filter. All data were acquired using Sweep-Me! as control software for automated measurement protocols.<sup>[31]</sup>

The PL of the sample is recorded using a UV–vis spectrometer for monitoring purposes only and is not required for further data analysis. Figure 2a illustrates how the CW-excited PL spectra depend on excitation wavelength. At 300 nm, both the phosphorescent BP-2TA and fluorescent QD emission characteristics are visible (green line), as both molecular species absorb light of this wavelength. With increasing the excitation wavelength toward 420 nm (yellow to red line color), the RTP emission vanishes, as the excitation light only overlaps with the falling flank of its absorbance tail. As a result, the relative share of RTP emission decreases, and the proportion of QD emission increases. Since the triplet decay time of BP-2TA is on the millisecond scale, this luminescence transition can be monitored by detecting the off-cycle PL intensity with a PD. The data are normalized to the average on-cycle PL under CW excitation (shutter open) and thus express the share of phosphorescence to total luminescence. Figure 2c depicts such transients (ten averages each) for an excitation wavelength sweep from 300 to 420 nm. The PL plateau is recorded under CW excitation (shutter open). Here, all radiative exciton recombination pathways can be seen ( $T_{RTP}$ ,  $S_{RTP}$ , and  $S_{QD}$ ). With the shutter being closed, the excitation light ceases and the pure RTP afterglow is visible. Consequently, the onset of the off-cycle PL transient sets a measure for the SMR. With increasing excitation wavelength, the afterglow intensity is reduced, as a fewer BP-2TA triplets get excited. At the same time, the QD emission prevails due to their stable absorbance characteristics. As a result, the relative share of excited triplet excitons is reduced and the SMR decreases. Under the condition of moderate excitation intensity and nonlinear exciton dynamics being negligible (see the reasoning in Section S4 in the Supporting Information), exciting the active film with an unknown wavelength within the sensing window thus results in a specific off-cycle transient that can be identified unambiguously with a distinct excitation wavelength.

Two issues exacerbate the readout of the SMR in Figure 2c. First, the shutter closing takes several milliseconds. Thus, the excitation light quenching does not appear as a sharp edge in the graph, and the fluorescence contribution does not vanish

immediately. Consequently, the time at which the shutter was fully closed (indicated by the vertical black line in Figure 2c) was defined as the readout point for the afterglow intensity. The PL value at this point in time is called “afterglow intensity” and is displayed in Figure 3. Second, the spectral response of the detector needs to be taken into account. The external quantum efficiency (EQE) of the silicon PD is not exactly constant over wavelength, i.e., different photon energies are not equally represented in the transient. Because the emission spectrum of the PL film changes with excitation wavelength (cf., Figure 2a), this evaluation does not produce a true SMR value, but a distorted quantity, earlier defined as “afterglow intensity.” An approach

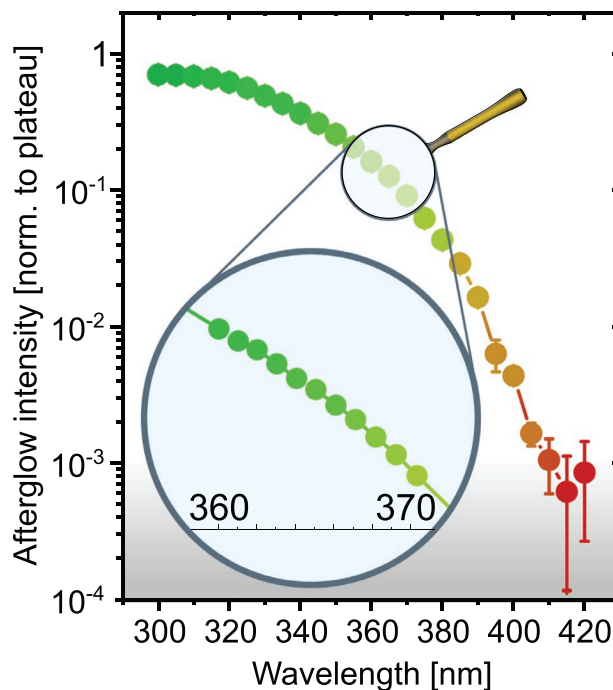


**Figure 3.** Wavelength identification by afterglow intensity. The afterglow intensity, as defined in the text, is plotted over excitation wavelength and produces a monotonous function. Beyond 410 nm of excitation wavelength, the sensor reaches its detectivity limit (indicated as a gray-shaded area) and cannot resolve wavelength changes anymore. The error bars indicate the standard deviation ( $n = 10$ ) of each measurement point.

addressing both topics is presented later in this manuscript when employing an all-organic device.

Despite these two issues, a monotonous function for unambiguous wavelength identification is achieved, ranging from 300 to about 410 nm (Figure 3). The insets in Figures 2 and 3 indicate that wavelength steps of 1 nm (and even in the following sections, see Section S6 in the Supporting Information) can be discriminated. Moreover, the system does not suffer from apparent hysteresis, as presented in Section S2 (Supporting Information). Figure 3 indicates the upper wavelength-sensing limit (detection limit, gray-shaded area), which is set by the PD's specific detectivity, the number of transient averages, and, not the least, the properties of the emitter materials blended into the PL film. With our settings being chosen as presented, we can discriminate wavelengths up to  $\approx 410$  nm.

### 2.3. Realizing an All-Organic Wavelength Sensor

Up to now, we have presented a solution-processed single active layer that discriminates wavelengths between 300 and 410 nm. Several readout and device issues have been addressed. We subsequently demonstrate how they can be tackled by changing distinct experimental settings. First, our idea aims at integrated systems, where a thin-film and flexible detector might be favored over a silicon PD. So, we subsequently use a DCV-5T:C<sub>60</sub> organic PD (OPD) instead of the silicon PD, as displayed in Figure 4a. Second, we show that cadmium-based QDs can be replaced by other nontoxic fluorophores, such as organic singlet emitters featuring appropriate absorption profiles. By blending 4-(dicyanomethylene)-2-*tert*-butyl-6-(1,1,7,7-tetramethyljulolidyl-9-enyl)-4*H*-pyran (DCJTb) instead of QDs into PMMA:BP-2TA, the system becomes prone to dual-state Förster resonance energy transfer (FRET). Both the excited triplet and singlet states of BP-2TA can transfer their energy efficiently to the singlet state of DCJTb.<sup>[32]</sup> This sensitized fluorescence renders both the film's prompt and delayed emissions for all excitation wavelengths to be of the same color.<sup>[12]</sup> While the QDs proved unsusceptible to Förster energy transfer from the RTP emitter, DCJTb was seen to accept BP-2TA's triplet and singlet energies quite efficiently (cf. Section S1, Supporting Information). We suspect the QD's oleic acid ligands together with the host polymer to effectively prevent nonradiative energy transfer by bridging the donor-acceptor distance, which relates to the transfer efficiency by the inverse sixth power.<sup>[33,34]</sup> Hence, DCJTb as singlet-emitting species solves the wavelength-dependent EQE problem of the PD issued above, which would have been of even greater significance when using an OPD.

As the elongated closing time of the mechanical shutter from Figure 2c induces distortions to the PL transients of our film, we now demonstrate that a faster switch-off directly translates into an improved transient signal. Electrically driven LEDs are installed as excitation sources instead. This leads to an immediate drop of excitation light and singlet emission intensity below the millisecond scale, as can be seen in Figure 4b. We obtain fewer observation points on the scale of excitation wavelength since we have only a limited number of LEDs at hand. Now, the plummeting excitation intensity allows us to read out a truly proportional SMR value from the onset of the afterglow transient.

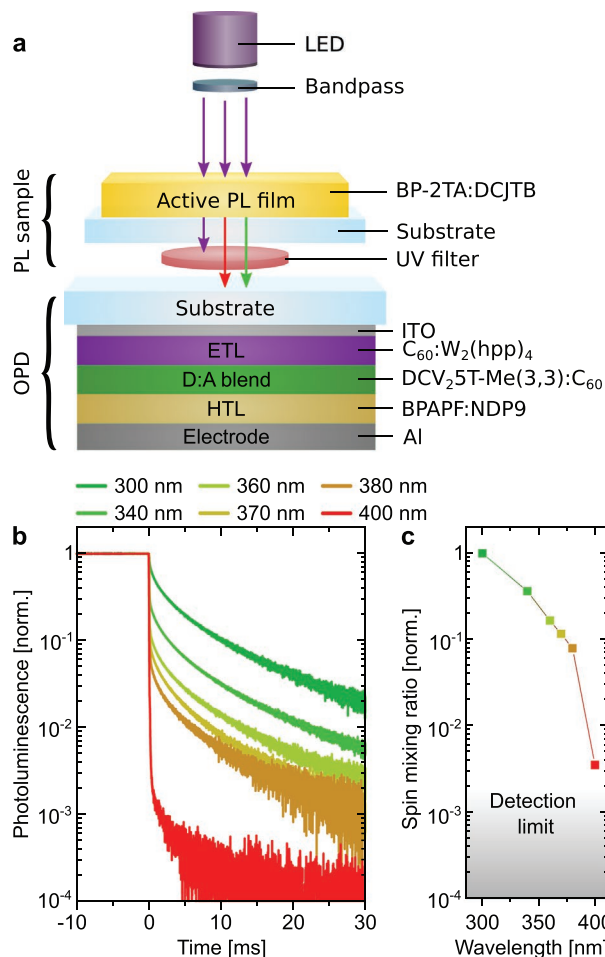


**Figure 4.** All-organic wavelength sensor. a) Sketch of the sensor stack (not drawn to scale); see the “Experimental Section” for details. b) The respective normalized transients ( $n = 10$ ) and c) the detected SMR. A steep singlet emission drop can be observed, owing to the faster switching of electrically driven LEDs that are used as excitation light sources.

### 2.4. Demonstration Scenarios for Wavelength Tracking

Beyond the conceptual proof of wavelength sensing by exciton spin mixing, two application scenarios are presented in this section, where a simple wavelength tracking system replaces a full spectrometer that would have been necessary otherwise. The experiments use the BP-2TA:QD film connected to the silicon PD equipped with a longpass UV filter.

In the first setup, the 365 nm LED from the former experiment is switched on in continuous mode for heating up. Using a calibrated, commercial spectrometer, we could determine that the LED peak wavelength shifts red by about 0.6 nm over 18 min while running at the maximum driving current of 700 mA. The specification sheet of the LED suggests that the case heating due to continuous operation induces this emission shift (see Section S8 in the Supporting Information). Performing a calibration measurement, this peak emission shift can be correlated to the PL afterglow intensity of the wavelength sensor (see Section S8 in the Supporting Information for details). A subsequent measurement can now track the LED emission



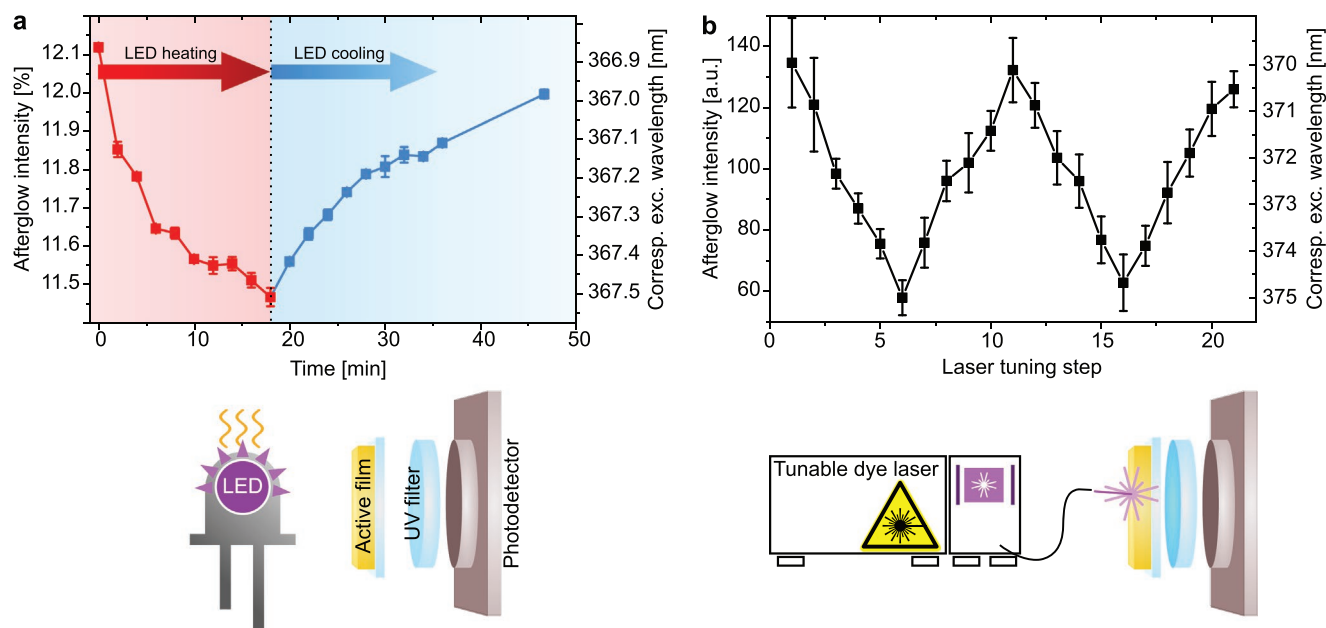


**Figure 5.** Demonstration of wavelength-tracking applications. a) Tracking of LED heating as well as cooling and the corresponding wavelength shift ( $n = 3$ ). b) Wavelength tracking of a tunable dye laser ( $n = 10$ ). The error bars indicate the standard deviation. Details can be found in Sections S8 and S9 (Supporting Information).

shift using the wavelength sensor only (Figure 5a). After 18 min of continuous driving, i.e., heating, the LED is turned off and rests for 30 min. Within these 48 min, the PL off-cycle response is measured every 2 min. A measurement cycle consists of three times switching the LED 300 ms on and 300 ms off and a subsequent averaging of the signals. Every measurement slightly disturbs the pure heating and cooling characteristics of the LED and hence is only repeated three times every 2 min. The heating and cooling characteristics of the LED are clearly resolved by our sensor.

For the second demonstration, a pulsed and tunable dye laser is used as an excitation source. Again, a calibration measurement enables an experiment, where the introduced wavelength sensor can be used to determine the emission wavelength of the laser (Figure 5b). The laser was tuned back and forth while measuring the PL response of the active film ten times and averaging. As the laser pulse is only about 1 ns long, the triplet density has only a little time to build up. Hence, the afterglow intensity is very weak. This yields a high standard deviation limiting the resolution to well above 1 nm at ten averages, although the laser wavelength is in the sweet spot of the system's resolution and the excitation intensity is quite high. The short excitation pulse does not produce a stable PL plateau to which the afterglow data can be normalized. Instead, it is normalized to the integral of the detected prompt PL burst of the film. Hence, the units of the afterglow intensity are only arbitrary. Details can be found in Section S9 (Supporting Information).

Both proof-of-concept experiments show clearly that the exciton spin mixing system is well capable to track the spectral intensity of a given light source and suggest that it can be particularly useful for simple monitoring tasks. Here, one will benefit from the low system complexity and cost.

### 3. Discussion and Perspectives

The two demonstrated tracking applications require calibration with the very same excitation source. First, the spectral shape of the light source influences the afterglow intensity characteristics, as not only the peak wavelength may determine the off-cycle response. As we present a simplistic 1D readout scheme, our sensor cannot discriminate between different spectral shapes. Second, the exposure time of the excitation source is crucial for whether the PL film reaches a steady state of excited triplet excitons. Any exposure time well above the lifetime of the triplet excitons will not change the afterglow intensity. However, as presented in the laser-tracking experiment, very short exposure times drastically reduce the afterglow intensity and hence the signal-to-noise ratio. In the case of monochromatic excitation and long exposure times, e.g., with a CW laser and shutter combination, where those issues do not arise, the calibration source can be different from the test source.

For the presented measurement concept, the boundaries of the sensitive interval and the spectral resolution are set by the absorbance characteristics of the fluorophores and phosphors embedded into the film. With the presented materials, we can scan an interval ranging from 300 to 410 nm and achieve a monotonously falling afterglow intensity, which in turn enables discrimination of excitation wavelengths within that range. In the steepest range of the afterglow intensity profile, a resolution down to 1 nm or below is achieved, depending on the experimental settings, like excitation intensity and averages (Section S6, Supporting Information). Use of phosphorescent molecules with red-edge absorption tails in different wavelength regimes, such as  $\text{BF}_2(\text{HPhN})$ ,<sup>[35]</sup>  $\text{BF}_2\text{bdks}$ ,<sup>[36]</sup> or  $\text{PhenTpa}$ ,<sup>[37]</sup> adopts the sensitivity range of the system according to the experimental purpose. Potential application scenarios, such

as monochromator calibration or laser wavelength tracking, might require high spectral resolution. This quantity relates closely to the absorption profile gradient of the RTP emitter (Section S6, Supporting Information). For such scenarios, it is feasible to employ phosphors with steep absorption edges, e.g., 2,2',7,7'-tetrakis(diphenylamino)-9,9'-spirobifluorene (Spiro-TAD),<sup>[38]</sup> 2,2',7,7'-tetra(*N,N*-di-*p*-tolyl)amino-9,9'-spirobifluorene (Spiro-TTB),<sup>[39]</sup> or 2,2',7,7'-tetrakis[*N,N*-di(4-methoxyphenyl)-amino]-9,9'-spirobifluorene (Spiro-OMe-TAD),<sup>[40]</sup> which are established, temperature-stable organic light-emitting diode (OLED) materials.<sup>[41–43]</sup> Also the optimized emitter concentration can change the required exciton dynamics, as scanned in ref. [24]. The PLQY of the emitting sites, the number of averages, and the sheer thickness of the active film are additional knobs that can be turned to increase the sensor's sensitivity. Sensitivity range and resolution are hence trade-offs that can be adjusted according to the particular application concept. This again emphasizes that the SMR response function is unique for every material system and that a sensing device requires initial calibration. Sensitivity range and resolution are hence trade-offs that can be adjusted according to the particular application concept.

Fluorescent quantum dots are easily scalable throughout the visible wavelength range and are therefore adaptable to any phosphorescent molecule, making them our composite of choice. To demonstrate an all-organic and cadmium-free device for versatile integration, we used a sensor employing an organic PD and organic fluorophore. It is also worth stressing that the wavelength-sensitive film itself can be physically decoupled from the electrically wired (O)PD. For applications in challenging surroundings, this might pay off. By chemical passivation or encapsulation, molecular emitters were also demonstrated stable under moist or ambient conditions.<sup>[44–47]</sup>

As mentioned above, the definition of the SMR is only valid while nonlinear effects are negligible. Using a high-power LED, we scanned a wide range of excitation intensities and determined the excitation sources used throughout the manuscript to cause no significant nonlinearity (Section S4, Supporting Information). This finding is accounted for by three main points: a heavily diluted RTP emitter (3 wt%), the polymer matrix, and finally the low triplet lifetime (30 ms), all of which cause a low triplet–triplet interaction probability. For further investigations comprising different RTP emitters, however, the onset of annihilation-induced nonlinearities above a certain excitation intensity threshold needs to be considered.

The most intense transients take about 250 ms to reach the detector's noise level with the material system used in our experiments. The PL film requires about the same time to achieve a steady level of excited triplet states under illumination. Hence, a rectangular light source driving voltage could be run at  $\approx 2$  Hz. This parameter, however, strongly depends on the phosphor's triplet lifetime and the readout procedure. Using an RTP emitter with a shorter lifetime in the microsecond range, e.g., 2,3,7,8,12,13,17,18-octaethyl-21H,23H-porphine platinum (PtOEP), would significantly enhance the potential readout speed. For data acquisition, we averaged every transient ten times. Another way could be the integration of a single transient. This reduces the susceptibility to noise, as not only one single value per transient is measured. This approach could

be beneficial in terms of readout speed since less or no averages need to be taken (cf., Section S3, Supporting Information). In contrast to the readout procedure in the time domain presented in this text, a red- and a green-sensitive stacked, dual-wavelength OPD<sup>[48]</sup> could be used to identify the PL contributions of singlet and triplet emitters, and hence determine the spin mixing ratio. This solution might be superior to the here-presented conception, as it accepts a continuous excitation light source, and is therefore currently investigated.

The spectral detectivity of the complete sensor system relates to parameters like the PLQY of the emitting molecules, incoupling efficiency of the film's PL into the PD, and finally the specific detectivity of the PD itself. It, therefore, offers a number of knobs to be turned in order to optimize the system for specified use cases. The presented wavelength tracking routine applies to a scenario where the excitation can be ceased on the millisecond scale using a shutter or an electric switch.

The wavelength sensor does not require any additional refractive elements. We had, however, to apply a wavelength longpass filter in front of the PD to cut off the remaining excitation light (cf., Figure S2b, Supporting Information). For a monolithic solution, we are currently developing thin-film filters that can be integrated into our thin-film processing techniques. Otherwise, either a suitable substrate may act as an excitation filter, or a grazing-angle experiment could be realized that limits the amount of excitation light. Moreover, we already presented efficient oxygen barrier layers that enable RTP applications in ambient atmosphere and can also be applied here.<sup>[24]</sup>

Finally, we conduct lifetime estimations of the active film. The results are presented in Section S11 (Supporting Information). Here, we stress the film with harsh UV conditions over 10 000 exposure cycles, corresponding to an accumulated dose of about  $13 \text{ kJ m}^{-2}$  at 365 nm. While the triplet lifetime remains stable, a slight degradation (about 1.5%) in the afterglow intensity is detected. Depending on the required accuracy, the sensor requires recalibration after being exposed to a certain UV dose.

## 4. Conclusion

We present the ability of wavelength sensing using a single PL film attached to a simple broadband detector. The pivotal idea is to specifically exploit the overlapping absorption profiles of fast- and slow-emitting molecules that are blended into the PL film, i.e., to selectively excite rather singlet or triplet excited states and, therefore, to control the spin mixing of the emitter system. By tracking their PL response, the readout is solely conducted in the time domain by transforming wavelength information into a distinct, monotonous afterglow intensity function. This is by no means the standard solution for processing spectroscopic data but is an exceptional physical concept. The presented sensor does not require diffractive elements and can scan a spectral range of about 100 nm with a maximum resolution of  $<1$  nm. It does not compete with full spectrometers but can facilitate wavelength measurements in integrated systems, such as monochromator calibration or laser wavelength tracking. An all-organic solution based on an organic PD is presented, demonstrating how such a sensor can be manufactured entirely from versatile components. We further discuss how the

choice of emitting materials sets the frame for adapting spectral resolution and sensitive range for individual purposes and finally demonstrate heating-induced LED emission shifts and laser wavelength tracking as two application scenarios.

## 5. Experimental Section

**Film Preparation:** The active film was consisted of a simple host-guest system that was drop-cast from solution onto an inch-by-inch quartz glass substrate. PMMA was used as the host material (average molecular weight 550 000 u, purchased from Alfa Aesar) dissolved in anisole (80 mg mL<sup>-1</sup>). The RTP emitter BP-2TA was synthesized as described in ref. [23] and dissolved in anisole (10 mg mL<sup>-1</sup>). The organic fluorophore DCJTB (purchased from Sigma-Aldrich) was dissolved in anisole (10 mg mL<sup>-1</sup>). The CdSe/CdS quantum dots were synthesized as described in ref. [25] and dissolved in toluene. All solutions were stirred for 2 h on a hotplate set to 50 °C. For preparing the final solution, 400 μL of PMMA solution (58 nmol of PMMA, >96 wt%), 100 μL of BP-2TA solution (1625 nmol of BP-2TA, 3 wt%), and either 5 μL of QD solution (125 pmol of QDs) or 10 μL of DCJTB solution (220 nmol of DCJTB, 0.3 wt%) were mixed. After further stirring, the films were drop-cast and left for drying in a fume hood overnight.

**Spectroscopic and Photocurrent Data Acquisition:** All data were acquired under nitrogen atmosphere. The edge emission spectra and photo transients were taken using a UV-vis spectrometer (CAS 140CTS, Instrument Systems) and an amplified silicon photodiode (PDA100A, Thorlabs) or self-fabricated organic photodiode with a current amplifier (Femto, DLPCA-200) using a multifunctional lab instrument (STEMlab 125-14, Red Pitaya) and Sweep-Me! as control software for automated measurement protocols.<sup>[31]</sup> The excitation source was operated for 300 ms (on-cycle) and rested for another 300 ms (off-cycle) for every measurement. This was ten times the triplet lifetime of the organic phosphor and ensured a stable triplet density. The PL transients were averaged ten times. As a light source, a xenon white-light source (LOT Quantum Design LSH-302) and monochromator (Bentham MSH-300, Quantum Design) with an attached optical beam shutter (SH05, Thorlabs) were used. The monochromator uses two gratings within the wavelength region of interest ( $\lambda \leq 395$  nm: MSG-T-2400-250 with 2400 mm<sup>-1</sup>,  $\lambda > 395$  nm: MSG-T-1200-500 with 1200 mm<sup>-1</sup>). The specifications for the 1200 mm<sup>-1</sup> grating were a resolution of <0.3 nm, an accuracy of  $\pm 0.2$  nm, and a reproducibility of  $\pm 0.05$  nm.<sup>[49]</sup> In the case of the all-organic sensor, four different mounted LEDs (Thorlabs M300L4, M340L4, M365L2,<sup>[50]</sup> and M405L3) were used. Except for the 300 nm LED, all of them were equipped with respective bandpass filters (FB340-10, FB360-10, FB370-10, FB380-10, and FB400-10 from Thorlabs) to achieve six excitation wavelengths. Absorbance spectra were taken using a spectral photometer UV-3100 (Shimadzu Deutschland). The 337 nm nitrogen laser (MNL 200, 200 kW excitation pulse power, 1 Hz frequency, 700–1000 ps pulse length) was fabricated by Lasertechnik Berlin and equipped with a tunable dye module (ATM, butyl-phenyl-biphenyloxydiazole (PBD) in toluene, concentration of  $4 \times 10^{-3}$  M).

**OPD Fabrication:** The layers of the OPDs were thermally evaporated in a vacuum system (Kurt J. Lesker Company Ltd., USA) at ultrahigh vacuum (base pressure of  $<10^{-7}$  mbar) on a glass substrate with a prestructured indium-tin-oxide (ITO) contact (Thin Film Devices). The substrate was cleaned in a multistep wet process including rinsing with *N*-methyl-2-pyrrolidone, ethanol, and deionized water as well as treatment with ultraviolet ozone. Details on the layer sequence are listed in Table S1 and Section S5 (Supporting Information). All organic materials were purified one to two times by gradual sublimation. The device area is defined by the geometrical overlap of the bottom and the top contact and equals 6.44 mm<sup>2</sup>. To avoid exposure to ambient conditions, the organic part of the OPD was covered by a small, transparent glass substrate, which was glued on top by employing a UV light curing epoxy resin (Denatite XNR 5592, Nagase & Co. Ltd, Japan).

**Statistical Analysis:** For transient acquisition, ten measurements were taken at each experimental setting yielding one averaged data set. The background (average of noise level) of every single transient was subtracted, and the data were normalized to the average of the PL plateau (excitation light on). When the excitation source was fully ceased, the transient intensity at this specific point in time was taken for all transients, referred to as “afterglow intensity.” This specific readout time was arbitrarily chosen according to the excitation light characteristics but remained unaltered for all data-processing steps. The ten afterglow intensity values in every data set were averaged. Figures 3–5 depict the mean value of each data set with the error bars being the respective standard deviation. The experiment of LED heating (Figure 5a) and the long-term measurement (Figure S11, Supporting Information) were taken with three averages to gain better temporal resolution.

## Supporting Information

Supporting Information is available from the Wiley Online Library or from the author.

## Acknowledgements

The authors thank Axel Fischer for contributing Sweep-Me! device classes that were necessary for automated measurement protocols. This work received funding from the European Research Council under the European Union’s Horizon 2020 research and innovation program (Grant Agreement No. 679213; project acronym BILUM). A.K. received funding from the Cusanuswerk Foundation and acknowledges funding from the DFG project HEFOS (Grant No. FI 2449/1-1). J.B. acknowledges the DFG project VA 1035/5-1 (Photogen) and the Sächsische Aufbaubank through Project No. 100325708 (InfraKart).

Open access funding enabled and organized by Projekt DEAL.

## Conflict of Interest

The authors declare no conflict of interest.

## Authors Contribution

Conceptualization: A.K. and S.R.; methodology: A.K., T.B., T.A., J.B., and F.F.; investigation: A.K., T.B., R.W., F.F., T.A., M.G., C.G., J.B., A.T.; visualization: A.K., M.G.; funding acquisition: A.K., J.B., K.L., A.E., S.R., M.G.; project administration: A.K., S.R.; supervision: A.E., K.L., S.R.; writing—original draft: A.K., J.B.; and writing—review and editing: all.

## Data Availability Statement

The data that support the findings of this study are available from the corresponding author upon reasonable request.

## Keywords

colloidal quantum dots, dual-state Förster resonance energy transfer, organic room-temperature phosphorescence, organic wavelength sensors, transient photocurrent

Received: June 2, 2022

Revised: July 20, 2022

Published online:

- [1] R. D. Jansen-Van Vuuren, A. Armin, A. K. Pandey, P. L. Burn, P. Meredith, *Adv. Mater.* **2016**, *28*, 4766.
- [2] W. Qarony, M. Kozawa, H. A. Khan, M. I. Hossain, A. Salleo, Y. H. Tsang, J. Y. Hardeberg, H. Fujiwara, D. Knipp, *Adv. Mater. Interfaces* **2020**, *7*, 2000459.
- [3] M. I. Hossain, H. A. Khan, M. Kozawa, W. Qarony, A. Salleo, J. Y. Hardeberg, H. Fujiwara, Y. H. Tsang, D. Knipp, *ACS Appl. Mater. Interfaces* **2020**, *12*, 47831.
- [4] Z. Yang, T. Albrow-Owen, W. Cai, T. Hasan, *Science* **2021**, *371*, eabe0722.
- [5] B. Siegmund, A. Mischok, J. Benduhn, O. Zeika, S. Ullbrich, F. Nehm, M. Böhm, D. Spoltore, H. Fröb, C. Körner, K. Leo, K. Vandewal, *Nat. Commun.* **2017**, *8*, 15421.
- [6] J. Xue, Z. Zhu, X. Xu, Y. Gu, S. Wang, L. Xu, Y. Zou, J. Song, H. Zeng, Q. Chen, *Nano Lett.* **2018**, *18*, 7628.
- [7] A. Armin, R. D. Jansen-Van Vuuren, N. Kopidakis, P. L. Burn, P. Meredith, *Nat. Commun.* **2015**, *6*, 6343.
- [8] M. Ebermann, N. Neumann, K. Hiller, M. Seifert, M. Meinig, S. Kurth, *Proc. SPIE* **2016**, 9760, 97600H.
- [9] J. Bao, M. G. Bawendi, *Nature* **2015**, *523*, 67.
- [10] V. Gautam, M. Bag, K. S. Narayan, *J. Am. Chem. Soc.* **2011**, *133*, 17942.
- [11] N. Ganesh, R. Shivanna, R. H. Friend, K. S. Narayan, *Nano Lett.* **2019**, *19*, 6577.
- [12] N. A. Kukhta, M. R. Bryce, *Mater. Horiz.* **2021**, *8*, 33.
- [13] M. Gmelch, H. Thomas, F. Fries, S. Reineke, *Sci. Adv.* **2019**, *5*, eaau7310.
- [14] Y. Zhou, W. Qin, C. Du, H. Gao, F. Zhu, G. Liang, *Angew. Chem., Int. Ed.* **2019**, *58*, 12102.
- [15] M. S. Kwon, D. Lee, S. Seo, J. Jung, J. Kim, *Angew. Chem.* **2014**, *126*, 11359.
- [16] Y. Liu, S. Tang, J. Fan, E. Gracia-Espino, J. Yang, X. Liu, S. Kera, M. Fahlman, C. Larsen, T. Wågberg, L. Edman, J. Wang, *ACS Appl. Nano Mater.* **2021**, *4*, 1162.
- [17] M. Adam, T. Erdem, G. M. Stachowski, Z. Soran-Erdem, J. F. L. Lox, C. Bauer, J. Poppe, H. V. Demir, N. Gaponik, A. Eychmüller, *ACS Appl. Mater. Interfaces* **2015**, *7*, 23364.
- [18] B. Ehrler, M. W. B. Wilson, A. Rao, R. H. Friend, N. C. Greenham, *Nano Lett.* **2012**, *12*, 1053.
- [19] M. Albaladejo-Siguan, D. Becker-Koch, A. D. Taylor, Q. Sun, V. Lami, P. G. Oppenheimer, F. Paulus, Y. Vaynzof, *ACS Nano* **2020**, *14*, 384.
- [20] D. Becker-Koch, M. Albaladejo-Siguan, Y. J. Hofstetter, O. Solomeshch, D. Pohl, B. Rellinghaus, N. Tessler, Y. Vaynzof, *ACS Appl. Mater. Interfaces* **2021**, *13*, 18750.
- [21] Y. Shirasaki, G. J. Supran, M. G. Bawendi, V. Bulovič, *Nat. Photonics* **2013**, *7*, 13.
- [22] X. Fan, D. Knepe, V. Sayevich, H. Kleemann, A. Tahn, K. Leo, V. Lesnyak, A. Eychmüller, *J. Phys. Chem. Lett.* **2019**, *10*, 4025.
- [23] A. Tomkeviciene, A. Dabulienė, T. Matulaitis, M. Guzauskas, V. Andruleviciene, J. V. Grazulevicius, Y. Yamanaka, Y. Yano, T. Ono, *Dyes Pigm.* **2019**, *170*, 107605.
- [24] M. Gmelch, T. Achenbach, A. Tomkeviciene, S. Reineke, *Adv. Sci.* **2021**, *8*, 2102104.
- [25] C. Guhrenz, V. Sayevich, F. Weigert, E. Hollinger, A. Reichhelm, U. Resch-Genger, N. Gaponik, A. Eychmüller, *J. Phys. Chem. Lett.* **2017**, *8*, 5573.
- [26] S. Hirata, K. Totani, J. Zhang, T. Yamashita, H. Kaji, S. R. Marder, T. Watanabe, C. Adachi, *Adv. Funct. Mater.* **2013**, *23*, 3386.
- [27] H. Thomas, K. Haase, T. Achenbach, T. Bärschneider, A. Kirch, F. Talmack, S. C. B. Mannsfeld, S. Reineke, *Front. Phys.* **2022**, *10*, 841413.
- [28] M. Gmelch, *Ph.D. Thesis*, Technische University Dresden, Germany **2021**.
- [29] Y. Tian, T. Newton, N. A. Kotov, D. M. Guldi, J. H. Fendler, *J. Phys. Chem.* **1996**, *100*, 8927.
- [30] G. D. Scholes, *Adv. Funct. Mater.* **2008**, *18*, 1157.
- [31] A. Fischer, F. Kaschura, SweepMe! GmbH, A multi-tool measurement software (2020), www.sweep-me.net (accessed: March 2022).
- [32] A. Kirch, M. Gmelch, S. Reineke, *J. Phys. Chem. Lett.* **2019**, *10*, 310.
- [33] S. E. Braslavsky, E. Fron, H. B. Rodríguez, E. S. Román, G. D. Scholes, G. Schweitzer, B. Valeur, J. Wirz, *Photochem. Photobiol. Sci.* **2008**, *7*, 1444.
- [34] Th. Förster, *Radiat. Res., Suppl.* **1960**, *2*, 326.
- [35] P. Lehner, C. Staudinger, S. M. Borisov, I. Klimant, *Nat. Commun.* **2014**, *5*, 4460.
- [36] C. A. Derosa, S. Hiroto, C. L. Fraser, *J. Phys. Chem. C* **2019**, *123*, 20488.
- [37] M. Louis, H. Thomas, M. Gmelch, A. Haft, F. Fries, S. Reineke, *Adv. Mater.* **2019**, *31*, 1807887.
- [38] C. Isenberg, T. P. I. Saragi, *J. Mater. Chem. C* **2014**, *2*, 8569.
- [39] C. Murawski, C. Fuchs, S. Hofmann, K. Leo, M. C. Gather, *Appl. Phys. Lett.* **2014**, *105*, 113303.
- [40] N. Onozawa-Komatsuzaki, T. Funaki, T. N. Murakami, S. Kazaoui, M. Chikamatsu, K. Sayama, *Electrochemistry* **2017**, *85*, 226.
- [41] F. Steuber, J. Staudigel, M. Stössel, J. Simmerer, A. Winnacker, H. Spreitzer, F. Weissörtel, J. Salbeck, *Adv. Mater.* **2000**, *12*, 130.
- [42] A. Kirch, A. Fischer, M. Liero, J. Fuhrmann, A. Glitzky, S. Reineke, *Light: Sci. Appl.* **2020**, *9*, 5.
- [43] A. Kirch, A. Fischer, M. Liero, J. Fuhrmann, A. Glitzky, S. Reineke, *Adv. Funct. Mater.* **2021**, *31*, 2106716.
- [44] Y. Gao, H. Zhang, Y. Jiao, W. Lu, Y. Liu, H. Han, X. Gong, S. Shuang, C. Dong, *Chem. Mater.* **2019**, *31*, 7979.
- [45] S. Kuila, S. J. George, *Angew. Chem.* **2020**, *132*, 9479.
- [46] G. Jiang, C. Guhrenz, A. Kirch, L. Sonntag, C. Bauer, X. Fan, J. Wang, S. Reineke, N. Gaponik, A. Eychmüller, *ACS Nano* **2019**, *13*, 10386.
- [47] M. Louis, H. Thomas, M. Gmelch, F. Fries, A. Haft, J. Lindenthal, S. Reineke, *Adv. Opt. Mater.* **2020**, *8*, 2000427.
- [48] Y. Wang, B. Siegmund, Z. Tang, Z. Ma, J. Kublitski, S. Xing, V. C. Nikolis, S. Ullbrich, Y. Li, J. Benduhn, D. Spoltore, K. Vandewal, K. Leo, *Adv. Opt. Mater.* **2021**, *9*, 2001784.
- [49] MSH-300 Specification Sheet.
- [50] M365L2 Specification Sheet.